Journal of Luminescence 282 (2025) 121247

Contents lists available at ScienceDirect

Journal of Luminescence

journal homepage: www.elsevier.com/locate/jlumin

Full Length Article

Effect of the deposition method on the luminescent properties of PMMA films doped with Eu^{3+} complexes containing amoxicillin drug ligand

Andrei Marcelino Sá Pires Silva [a], Airton Germano Bispo-Jr [b], Fernando Aparecido Sigoli [c], Carolina Ferreira de Matos Jauris [d], Ernani Lacerda de Oliveira Neto [b], Breno Pannia Espósito [b], Lilian Lefol Nani Guariero [e], Pollyana da Silva Melo [e], Ricardo Oliveira Freire [f], Jorge Fernando Silva de Menezes [g,*]

[a] State University of Santa Cruz, Higher Council of Education, Research and Extension, 45662900, Ilhéus, BA, Brazil
[b] Department of Fundamental Chemistry, Institute of Chemistry, University of São Paulo, São Paulo, SP, 05508-000, Brazil
[c] State University of Campinas, Institute of Chemistry, Department of Inorganic Chemistry, 13083970, Campinas, SP, Brazil
[d] Federal University of Santa Maria, Department of Chemistry, 96570000, Santa Maria, RS, Brazil
[e] SENAI - Regional Department of Bahia, Integrated Center for Manufacturing and Technology, 41650010, Salvador, BA, Brazil
[f] Federal University of Sergipe, Center of Exact Sciences and Technology, Department of Chemistry, Pople Computational Chemistry Laboratory, 49107230, São Cristóvão, SE, Brazil
[g] Federal University of Recôncavo da Bahia, Teacher Training Center / CFP, 45300000, Amargosa, BA, Brazil

ARTICLE INFO

Keywords:
Europium
Thin films
Lanthanide
β-diketone
β-lactam

ABSTRACT

The research on the development of luminescent polymer films often overlooks the impact of variations in deposition method factors on the properties of the films, particularly their spectral properties. This study aims to investigate the effects of concentration, dopant complex, and deposition methods drop casting and spin coating on the properties of luminescent films in PMMA matrix doped with europium (III) complexes, $[Eu(tta)_3(H_2O)_2]$ and $[Eu(tta)_3(amx)]$, and how these variables affect their spectral properties. Techniques such as infrared spectroscopy, hydrogen nuclear magnetic resonance spectroscopy, thermogravimetry, UV–Vis electronic absorption spectroscopy, excitation and emission spectroscopy, scanning electron microscopy, and atomic force microscopy were used, with a focus on spectral characterization. The results indicate that the produced films have significant potential for applications in photoluminescent labeling, UV radiation monitoring, optoelectronic devices, and other luminescent material systems.

1. Introduction

The interest in elements of the lanthanide series has grown in recent years due to their peculiar properties. With the development of more sophisticated separation methods in the mid-20th century [1], these properties were studied and showed great potential for application in a range of technological innovations, especially in the society where dependence on optical and electronic devices has become established [2]. However, lanthanide complexes still present several negative effects that make their direct use in technologies unfeasible, such as low photostability, thermostability, and mechanical resistance [3,4]. To overcome these effects, incorporating the complexes into matrices is common [5,6].

In this context, polymeric matrices stand out as excellent hosts for lanthanide complexes due to their mechanical resistance, flexibility, ease of processing, thermal stability, high photostability, and low cost compared to other available matrices [5]. The most used polymer for photonic applications, polymethyl methacrylate (PMMA), exhibits transparency and flexibility on the produced films and the waveguide effect, wich can offer a positive optical response in the production of luminescent films. This has significant potential for use in the production of LCMDs (light-converting molecular devices), OLEDs, sensors and other devices [7,8].

Among the most common methods for producing doped polymer films are casting and spin coating [9–14]. Spin coating is widely recognized for its capability to produce uniform and thin films with precise thickness control, making it particularly suitable for applications that demand consistency and rapid production. This method facilitates

* Corresponding author.
E-mail address: jorge_fernando@ufrb.edu.br (J.F. Silva de Menezes).

https://doi.org/10.1016/j.jlumin.2025.121247
Received 18 November 2024; Received in revised form 19 March 2025; Accepted 9 April 2025
Available online 11 April 2025

Table 1
Mass, concentration, deposition method, dopant complex and codes of the produced films.

Deposition	Complex	Concentration	PMMA (mg)	Complex (mg)	Code
Casting	[Eu(tta)$_3$(H$_2$O)$_2$]	0.5 wt%	99.5	0.5	ETH-0.5
		1.0 wt%	99.0	1.0	ETH-1.0
		2.0 wt %	98.0	2.0	ETH-2.0
		5.0 wt %	95.0	5.0	ETH-5.0
Spin coating	[Eu(tta)$_3$(amx)]	0.5 wt %	99.5	0.5	ETA-0.5
		1.0 wt %	99.0	1.0	ETA-1.0
		2.0 wt %	98.0	2.0	ETA-2.0
		5.0 wt %	95.0	5.0	ETA-5.0

easy adjustment of parameters such as rotation speed and duration, allowing researchers to effectively tailor film properties. In contrast, casting offers significant versatility in simplicity and cost-effectiveness, which render it an attractive option for large-scale production, while the ability to incorporate additives during the casting process further can enhance the functionality of the resulting films.

However, the impact of varying factors in the film production process on the results obtained is not widely discussed. Many studies with PMMA films using Eu^{3+} complexes lead to discussion in sensitization, spectral behavior, enhancement and application of the luminescence, without determining the relevance of the chosen deposition method. Additionally, it is not clear which method and factors yield better results in terms of thickness, transparency, thermal stability, quantum yield, decay rates, and luminescence intensity, making a comprehensive study on these points necessary.

In this context, the present work aims to introduce a discussion on the effect of varying factors in the film production method based on the synthesis of a new luminescent complex, using Eu^{3+}, β-diketone 2-thenoyltrifluoroacetonate (tta), and the ligand amoxicillin (amx), due to his low cost and favorable structure for coordination. The study includes the production of photoluminescent PMMA films doped with the complexes [Eu(tta)$_3$(H$_2$O)$_2$] and [Eu(tta)$_3$(amx)], characterizing them in terms of structure, morphology, thermal analysis and spectroscopy, and analyzing how these factors influence the properties of the films.

2. Experimental section

2.1. Materials

Europium oxide (Sigma-Aldrich, 99.999 %), 2-thenoyltrifluoroacetone (Sigma-Aldrich, 99 %), hydrochloric acid (Merck, 37 %), acetone (Sigma-Aldrich, 99.5 %), pentane (Sigma-Aldrich, 98 %), ethyl acetate (Sigma-Aldrich, 99.5 %), ethanol (Sigma-Aldrich, 99.5 %), acetonitrile (Sigma-Aldrich, 99.9 %), dimethyl sulfoxide (Sigma-Aldrich, 99.9 %), poly(methyl methacrylate) (Sigma-Aldrich) and ammonium hydroxide (Sigma-Aldrich, 28–30 %) were used without prior purification. The amoxicillin ligand (Amoxicillin trihydrate) was obtained from the generic drug (Teuto, 250mg/5 mL) of the same name by solvent extraction to remove the excipient.

2.2. Synthesis of [Eu(tta)$_3$(H$_2$O)$_2$] (ETH)

The process for the synthesis of the complex [Eu(tta)$_3$(H$_2$O)$_2$] was carried out according to Ref. [15], from the mixture of europium chloride hexahydrate (EuCl$_3$.6H$_2$O) with the ligand 2-thenoyltrifluoroacetonate (tta$^-$). The solid was recrystallized from acetone and washed with pentane and dried in a vacuum.

[Eu(tta)$_3$(H$_2$O)]: orange crystalline powder, mp 145–150 °C; IV (ATR): ν 3611 (f), 3321 (f), 1599 (F), 1584 (F), 1537 (F), 1509 (F), 1459 (m), 1407 (F), 1354 (F), 1295 (F), 1248 (F), 1190 (F), 1131 (F), 1060 (F), 929 (m), 859 (m), 786 (F), 711(F), 680 (m) cm $^{-1}$;^{1}H NMR (300 MHz, acetone-d6): δ 0.59 (s, 1H), 4.14 (s, 8H), 5.52 (s, 1H), 6.31 (s, 1H), 7.18 (d, J = 4.7 Hz, 1H) ppm. Anal. Calcd. for EuC$_{24}$H$_{16}$F$_9$O$_8$S$_3$: Eu, 17.85; Eu Found, 17.49.

2.3. Synthesis of [Eu(tta)$_3$(amx)] (ETA)

[Eu(tta)$_3$(H$_2$O)$_2$] (170 mg) was dissolved in approximately 30 mL of ethanol, as well as the ligand amoxicillin (70 mg). After dissolution of the precursor and ligand, the reaction system was mixed and stirred under reflux for 4 h, at ~120 °C, until the formation of a precipitate. The solid was washed with ethanol and dried in a vacuum.

[Eu(tta)$_3$(amx)]: orange-red crystalline powder; IV (ATR): ν 3561 (f), 3537 (f), 3354 (m), 2918 (m), 1641 (m), 1606 (F), 1535 (F), 1507 (F), 1459 (m), 1408 (F), 1354 (m), 1293 (F), 1248 (m), 1189 (F), 1138 (F), 1058 (F), 931 (m), 857 (m), 786 (F), 743 (m), 717(F), 687 (m) cm $^{-1}$; NMR- ^{1}H (300 MHz, acetone-d6): δ 1.22 (t, J = 7.0 Hz, 1H), 1.91 (s, 1H), 2.25 (s, 7H), 2.33 (s, 5H), 5.93 (d, J = 2.9 Hz, 8H), 6.44–6.40 (m, 7H), 7.20 (d, J = 4.8 Hz, 7H), 7.37 (d, J = 8.0 Hz, 1H), 7.49 (t, J = 7.7 Hz, 1H), 7.74 (t, J = 7.1 Hz, 1H), 7.99 (d, J = 7.9 Hz, 1H), 8.54 (s, 1H) ppm. Anal. Calcd. for EuC$_{40}$H$_{31}$F$_9$N$_3$O$_{11}$S$_4$: Eu, 12.87; Eu Found, 12.94.

2.4. Film production

The films were fabricated by the drop casting or spin coating deposition methods. For each film, a mass of 0.1g of PMMA crystals were weighed, and a mass of the complex, relative to their proportion, was weighed added to the mixture, namely: 0.0005 g (0.5 wt %), 0.001 g (1 wt %), 0.002 g (2 wt %) and 0.005 g (5 wt %), with error of ±0.00001g. It was dissolved in 10 mL of chloroform/sodium acetate 6:4 solution, and added to the PMMA crystal, along with 20 mL of the solution and stirred for 1 h under heating (~100 °C). The composition of each film is shown in Table 1. Using the casting method, the homogeneous polymer solution was deposited in a Petri dish (diameter = 80 mm), to dry the film by evaporating the solvent overnight at room temperature (25 °C). Using the spin coating method, deposition was carried out via dynamic addition on a 2.5 cm × 2.5 cm glass substrate with a rotation of 2000 rpm, followed by evaporation of the solvent, which occurred overnight at room temperature (25 °C).

2.5. Methods

2.5.1. Photoluminescence spectra and luminescence decay

Photoluminescence spectra (PL) were obtained at 293 K in a Horiba Jobin-Yvon FL3-22-iHR-320 spectrofluorometer in front-face mode using a Xe lamp (450 W) as excitation source. All spectra were corrected according to the response of the photomultiplier (Hamamatsu PMT) and Xe lamp emission. Emission lifetime was recorded by using a time correlated single-photon counting (TCSPC) system (FluoroHub-B) linked with a pulsed 150 W Xenon lamp.

2.5.2. Scanning electron microscopy

Scanning Electron Microscopy data were obtained using a JEOL scanning electron microscope (SEM), JEOL Carry Scopy JSM-6510LV model, with acceleration voltage of 20 kV. FTIR spectra were obtained on a Bruker Vertex 70 spectrometer, equipped with a Platinum ® ATR (attenuated total reflectance) diamond crystal accessory, from 4000 to 30 cm^{-1}, resolution of 1 cm^{-1} and 64 accumulations.

2.5.3. Atomic force microscopy

Topographical atomic force microscopy images were performed on a Park NX10 microscope (Park Systems, Suwon - Korea). The Si tip

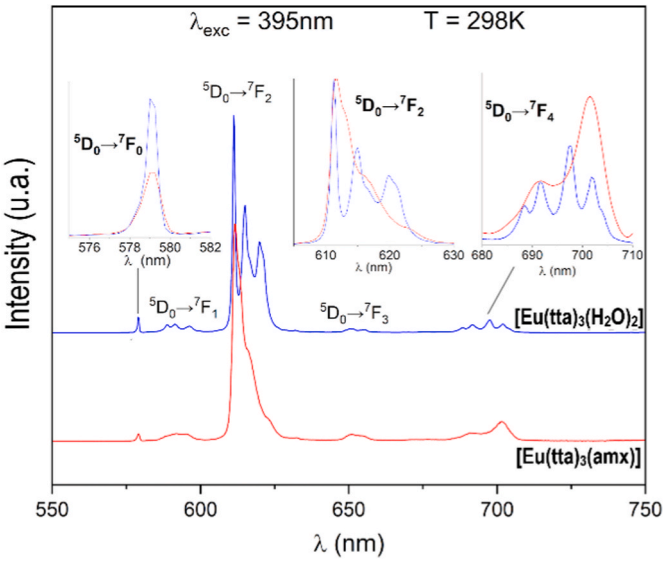

Fig. 1. Emission spectra of $[Eu(tta)_3(H_2O)_2]$ and $[Eu(tta)_3(amx)]$.

(Budget Sensors) used has a spring constant of 0.2 N m^{-1} and a nominal resonance frequency of 13 kHz. The images were processed using the XEI version 4.3.4 Build22.RTM1 software.

2.5.4. Thermal analysis

Thermal analysis data were used in a Thermogravimetry module model DTG-60H with capacity for differential and thermogravimetric analysis simultaneously (TGA/DTA) with a "TOP PLAN" type scale with parallel differential guide, in which 2–10 mg of powder were placed in an alumina crucible and heated to 1000 °C at an incremental rate of 10 °C min^{-1} under a nitrogen atmosphere with a flow rate of 100 mL min^{-1}. Melting point data were obtained on a Gehaka PF1000 apparatus.

2.5.5. Proton nuclear magnetic resonance

Samples for ^1H NMR were prepared by dissolving the compounds in acetone-d6, deuterated water or DMSO-d6, obtaining solutions with final concentrations of approximately 7.7 mg mL^{-1}. The spectra were obtained at 298 K on a Varian Inova 300 MHz equipment.

2.5.6. Transparency, absorption and transmittance data

The transparency of the films in percentage is obtained through a system using an LDR light sensor connected to a voltmeter and a green LED light connected to a 12 V source. Absorption and transmittance data were obtained on an UV–Vis Spectrophotometer Model GTA-97, in 10 $^{-4}$ M solutions in ethanol and ethyl acetate, scanning in the 190–800 nm region, with a 1 nm interval between data.

2.5.7. Complexometric titration

Lanthanide content analysis data were obtained by complexometric titration of the complexes, using 0.1 mol L^{-1} EDTA solution as a titrating agent and xylenol orange as an indicator. Finally, film thickness data were obtained using a caliper for films via casting and using the Swanepoel method for films produced via spin coating.

2.6. Theoretical study

2.6.1. Ground state geometries and excited state energies

The ground state geometries of the complexes $[Eu(tta)_3(H_2O)_2]$ and $[Eu(tta)_3(amx)]$ were calculated with the RM1 semiempirical quantum method [16,17]. The calculations were carried out in the MOPAC2016 software [18], version 18.117W with the following keywords: RM1; PRECISE; GNORM = 0.25; T = 10D; BFGS, GEO – OK and XYZ. The singlet and triplet ground state energies were calculated with the INDO/S-CIS (Intermediate Neglect of Differential Overlap/Spectroscopy – Configuration Interaction with single excitations) [19] method implemented in the ORCA program [20]. The RM1 geometry was used as input and the trivalent europium ion was treated as a +3e point charge.

2.6.2. Luminescent properties

The Judd-Ofelt intensity parameters (Ω_λ, λ = 2, 4 and 6); energy transfer (W_{ET}) and back transfer (W_{BT}) rates, radiative (A_{rad}) and non-radiative (A_{nrad}) emission rates, quantum efficiency (η) and quantum yield (q) were calculated in the LUMPAC program [21]. The procedure for calculating each of these quantities is detailed in the supplementary material – Section S1.

3. Results and discussion

3.1. Synthesis and characterization of the new Eu^{3+} complex

Qualitative and analytical characterization of the complexes are available at Tables S1–S3. FTIR spectra of the ligands Htta and amoxicillin as well as the complexes $[Eu(tta)_3(H_2O)_2]$ and $[Eu(tta)_3(amx)]$ are shown in Fig. S1. The complex $[Eu(tta)_3(amx)]$ presents the characteristic bands of the coordination of 2-thenoyltrifluoroacetone to the metal center, such as: C=O stretching band at 1604 cm^{-1} and C=C stretching band of enol at 1535 cm^{-1} [22–26]. The amine and amide stretching bands of amoxicillin do not change compared to the free ligand, indicating that there is no coordination with the metal center through any of the nitrogen sites. Both the C=O stretching bands of the β-lactam ring and amide on amoxicillin shifts to lower wavenumbers (~50-100 cm^{-1}), evidencing the coordination of amoxicillin to Eu^{3+} through these points [27–30]. The shifts of the IR bands can be observed in more details on Table S4.

^1H NMR spectra of the isolated ligands and complexes are available in Figs. S6–S9 in the supplementary material. The data for 2-thenoyltrifluoroacetone, amoxicillin and $[Eu(tta)_3(H_2O)_2]$ agree with those reported in the literature [31]. In $[Eu(tta)_3(amx)]$, the N–H proton of the amoxicillin ligand is displaced δ = 7.990 ppm, because of coordination via the amide carbonyl. Furthermore, the main peaks of free amoxicillin and coordinated 2-thenoyltrifluoroacetone are observed.

TG/DTG/DTA thermogravimetry curves of the synthesized complexes are shown in Fig. S10. The $[Eu(tta)_3(amx)]$ complex exhibits mass loss between 50 and 100 °C, evidence of presence of adsorption water, without coordination water in the structure, which has a higher decomposition temperature. The first thermal decomposition event associated with the structure of the complex occurs between 200 and 250 °C, associated with the decomposition of amoxicillin [32]. The most pronounced thermal event in both systems occurs in the range of 250 °C–350 °C, referring to the decomposition of the 2-thenoyltrifluoroacetone ligands [15,31]. Next, slow decomposition of the carbonaceous material occurs, and the formation of europium oxide happens between 400 and 850 °C, with a mass proportion of ~13 wt % from the initial mass, accordingly to the expected mass, measured by complexometric titration (Table S3).

The UV–Vis electronic absorption spectra measured in ethanol are shown in Fig. S11. Both materials have absorption bands between 250-300 nm and 300–400 nm, with a maximum absorption wavelength at 339 nm, referring to the π→π* transitions, associated with ligand 2-thenoyltrifluoroacetone. Furthermore, the addition of amoxicillin to the structure of the $[Eu(tta)_3(amx)]$ complex intensified the absorption in the region between 200 and 250 nm compared to the hydrated precursor complex, due to the π→π* transitions generated by the contribution of amx ligand.

The emission spectra of the powder complexes $[Eu(tta)_3(H_2O)_2]$ and $[Eu(tta)_3(amx)]$ are shown in Fig. 1, and it is possible to observe the occurrence of the $^5D_0 \rightarrow {}^7F_0$ transition in a single line, with a peak at 579

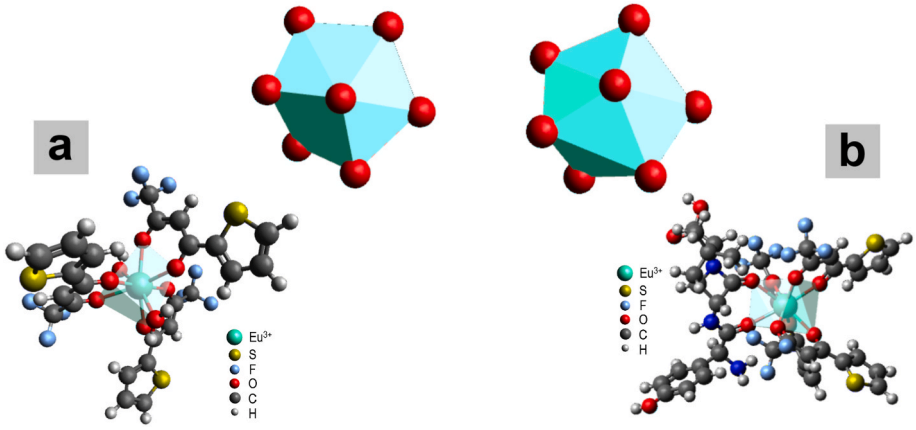

Fig. 2. Ground state geometries and coordination polyhedron of the complexes a) $[Eu(tta)_3(H_2O)_2]$ and b) $[Eu(tta)_3(amx)]$ calculated using the RM1 model.

Table 2
Spectral data of the complexes $[Eu(tta)_3(H_2O)_2]$ and $[Eu(tta)_3(amx)]$, with theoretical values in parentheses.

Sample	Ω_2 (10^{22} cm^2)	Ω_4 (10^{22} cm^2)	Ω_2^{ed} (10^{22} cm^2)	Ω_2^{dc} (10^{22} cm^2)	A_{rad} (s^{-1})
$[Eu(tta)_3(H_2O)_2]$	26.17(26.05)	6.44 (6.82)	0.1217	25.93	958.68 (934.73)
$[Eu(tta)_3(amx)]$	28.83 (28.82)	10.82 (10.84)	0.0165	28.80	1120.28 (1078.84)

Ω_λ: Judd-Ofelt intensity parameter.
Ω_2^{ed}: electron dipole Judd-Ofelt parameter.
Ω_2^{dc}: dynamic coupling Judd-Ofelt parameter.
A_{rad}: radiative decay rate.

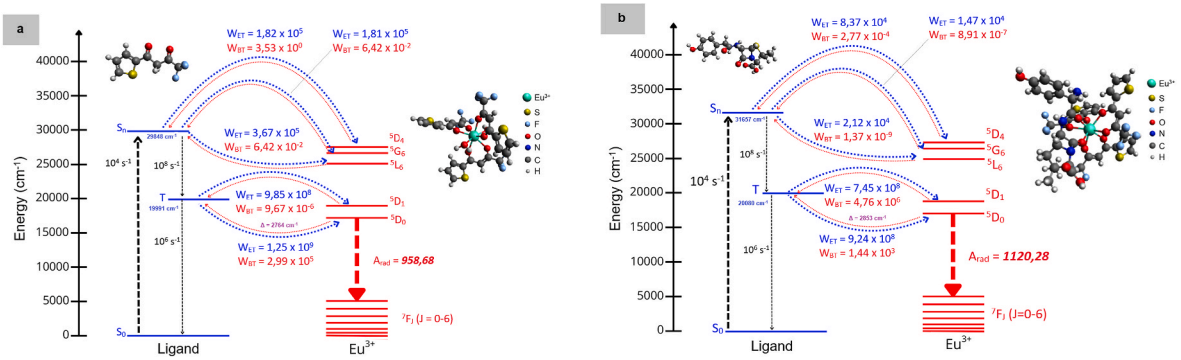

Fig. 3. Energy level diagram for the complexes a) $[Eu(tta)_3(H_2O)_2]$ and b) $[Eu(tta)_3(amx)]$.

nm, a phenomenon attributed to the absence of an inversion center in the local symmetry at the site of the metallic center. The $^5D_0 \rightarrow {}^7F_2$ band, hypersensitive to the local symmetry of Eu^{3+}, is the most intense in all systems, characterizing the red color emission. Comparing to the hydrated precursor, the $[Eu(tta)_3(amx)]$ exhibits a more resolved $^5D_0 \rightarrow {}^7F_2$ band, due to the stronger interaction of the Eu^{3+} ion with amx ligand through bidentate chelation, which reinforce the bond strenght and, consequently, also due to the dipole momentum of the ligand, improve the rigidity of the entire structure, as can be seen at Table S5 on the values of bond length and polarizability of Eu^{3+} ion and ligand atoms. Another interesting feature is the increase in relative intensity and the change in the profile of the $^5D_0 \rightarrow {}^7F_4$ transition in the system with amoxicillin. Occurring through forced electric dipole mechanisms, the $^5D_0 \rightarrow {}^7F_4$ transition is dependent on the chemical environment around Eu^{3+}, mainly on structure rigidity effects, which promoted the profile change observed in $[Eu(tta)_3(amx)]$, reinforcing the effect of structural changes which the incorporation of amx ligand promoted on the luminescent properties of the complex.

3.2. Theoretical study of the new complex $[Eu(tta)_3(amx)]$

The structure and geometry of the complexes $[Eu(tta)_3(H_2O)_2]$ and $[Eu(tta)_3(amx)]$ were obtained using the RM1 model [16,17]. The RM1 basis set is composed of 5d, 6s, and 6p orbitals, for a total of 9 orbitals and was parameterized to replicate crystallographic structures of systems containing trivalent lanthanide ions. The spherical coordinates of the coordination polyhedron, charge factors (g) and polarizabilities (α) of the atoms directly bonded to the Eu^{3+} ion are presented in Table S5 of the supplemental material. Fig. 2 shows the ground state geometry of both systems calculated with the RM1 method.

The complex $[Eu(tta)_3(amx)]$, has in its structure Eu^{3+} coordinated to three ligands tta^- in a bidentate way and an amoxicillin ligand linked in a bidentate way through the amide oxygens and the β-lactam ring, with coordination number equal to 8.

In systems with Fe^{3+}, Co^{2+}, Ni^{2+}, Cu^{2+} [33] and La^3, Ce^{3+}, Dy^{3+}, Y^{3+} [34], amoxicillin was coordinated in a tridentate mode through the amine, amide nitrogens and amide oxygen. In the system under study, $[Eu(tta)_3(amx)]$, the amoxicillin ligand is used as a secondary ligand, since the metallic center is already coordinated with three ligands tta^-,

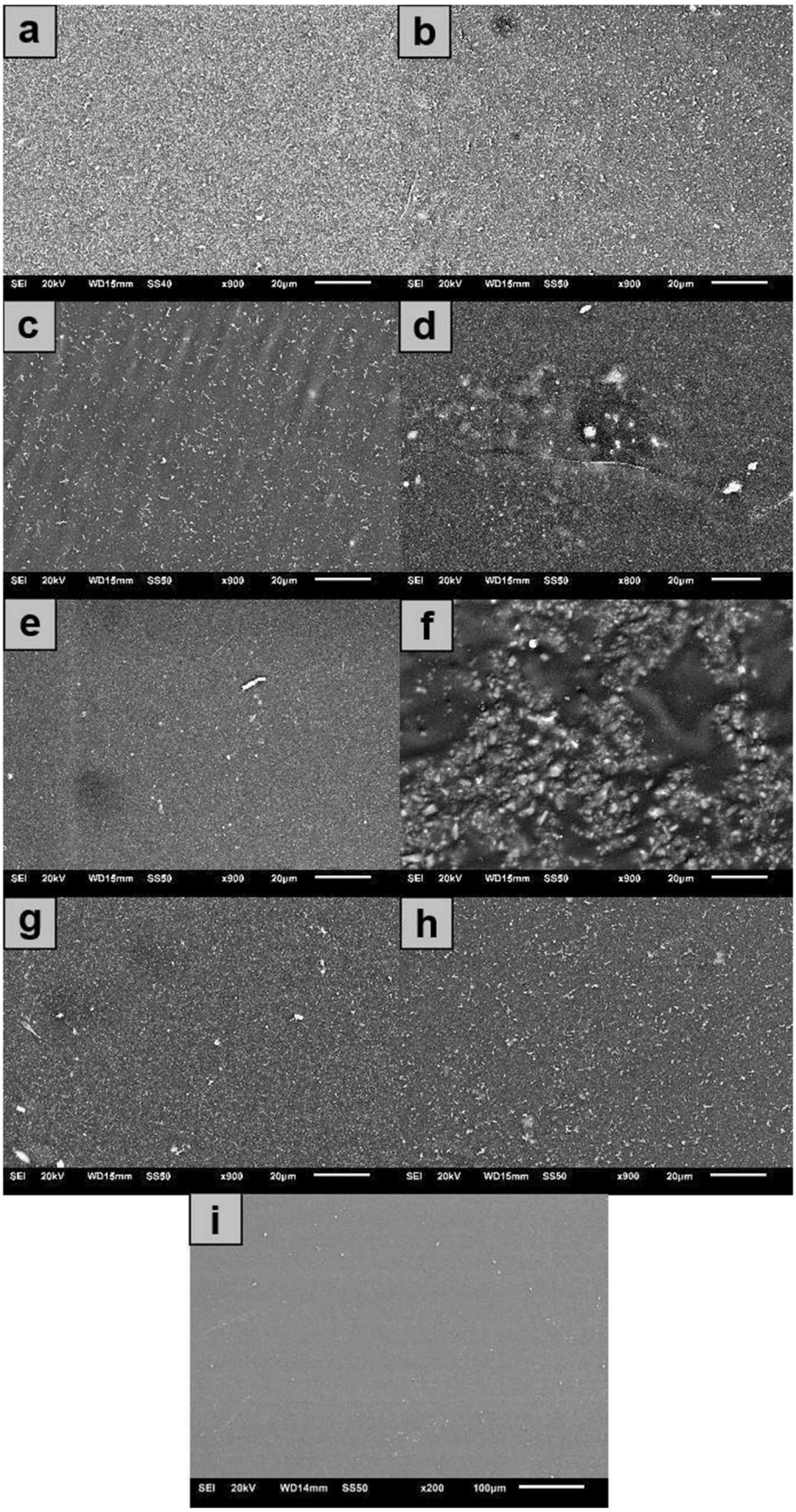

Fig. 4. Scanning electronic microscopy of the casting films a) ETH(C)-0.5; b) ETH(C)-1.0; c) ETH(C)-2.0; d) ETH(C)-5.0; e) ETA(C)-0.5; f) ETA(C)-1.0; g) ETA(C)-2.0, h) ETA(C)-5.0.

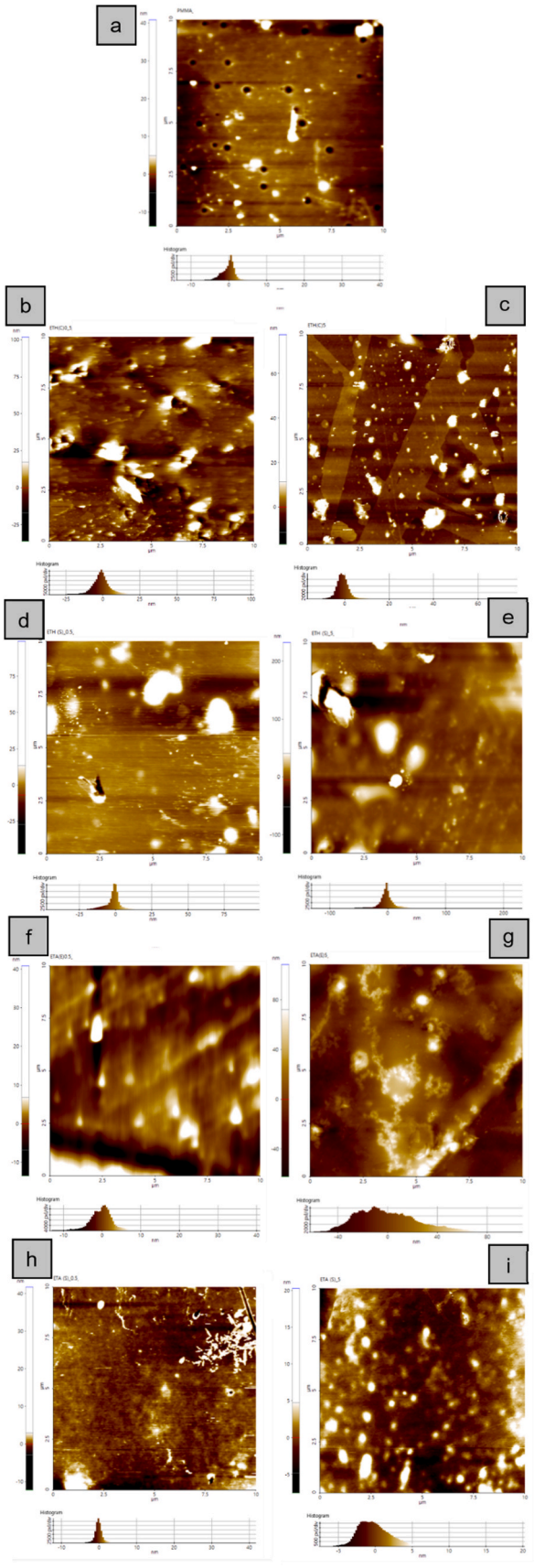

Fig. 5. Atomic Force Microscopy of the films a) without complex; b) ETH(C)-0.5; c) ETH(C)-5.0; d) ETA(C)-0.5; e) ETA(C)-5.0; f) ETH(S)-0.5; g) ETH(S)-5.0; h) ETA(S)-0.5; I) ETA(S)-5.0.

Table 3
Quadratic roughness data (R_q) and thickness of the polymeric films.

Sample	Rq (nm)	Thickness (μm)
PMMA	2.5	- - -
ETH (C) 0.5	8.7	40
ETH (C) 5.0	5.8	40
ETH(S) 0.5	10.3	0.59
ETH(S) 5.0	21.9	6.83
ETA (C) 0.5	3.5	130
ETA (C) 5.0	25.3	60
ETA(S) 0.5	1.5	0.86
ETA(S) 5.0	2.4	4.48

which produce a large steric hindrance, inducing coordination of the new ligand in bidentate mode.

The theoretical absorption data calculated with the INDO/S-CIS method generated absorption spectra similar to those observed experimentally, as could be observed in Fig. S11. The theoretical absorption spectrum of $[Eu(tta)_3(amx)]$ shows a hypsochromic shift of the maximum absorption wavelength compared to the precursor system, $[Eu(tta)_3(amx)$, occurring at 315.9 nm, with energy of 31657.4 cm^{-1}, related to the coordination of the amoxicillin ligand; in addition to this, another band was also observed at 231.5 nm, with energy of 43198.9 cm^{-1}.

Thus, together with the structural analyses, the semiempirical calculations justify the proposed structure for the complex $[Eu(tta)_3(H_2O)_2]$, already cataloged in the literature [15] and, mainly, the complex $[Eu(tta)_3(amx)]$. The spectral data obtained experimentally and theoretically are shown in Table 2.

The intensity parameter Ω_2, is quite high in both systems, with increase in $[Eu(tta)_3(amx)]$ compared to $[Eu(tta)_3(H_2O)_2]$ in the order of 2,63 x 10^{-20} cm^2, resulting from the increase in polarizability around the metallic center and intensification of the covalent character in the interactions between Eu^{3+} and, particularly, the contribution of the amoxicillin ligand. The polarizability data attest that the coordination of amoxicillin changed the structure at the symmetry site around the metal and modified the chemical environment, increasing the polarizability of the system, which justifies the intensification of the parameter Ω_2, which is strictly dependent on local symmetry. This effect is expected, since amoxicillin ($\mu = 3.58D$) [35] has a dipole moment greater than water ($\mu = 1.85D$) and therefore generates interactions with a high covalent character with the hard acid Eu^{3+}. It was also observed that the $[Eu(tta)_3(amx)]$ complex produced an increase in the dynamic coupling contribution to the $^5D_0 \rightarrow {}^7F_2$ transition, with a contribution of 99.94 %, compared to the hydrated precursor complex $[Eu(tta)_3(H_2O)_2]$, whose contribution is 99.54 %.

Energy level diagrams for both complexes are shown in Fig. 3, and energy transfer rates are available on Table S6. Both complexes present the predominance of the exchange mechanism ($T_1 \rightarrow {}^5D_1$ and $T_1 \rightarrow {}^5D_0$) on the energy transfer rate [2]. The singlet and triplet levels calculated using the INDO/S-CIS method of both complexes are, respectively: $S_n = 31657$ cm^{-1} and $T = 20080$ cm^{-1} for the complex $[Eu(tta)_3(amx)]$ and $S_n = 29848$ cm^{-1} and $T = 19991$ cm^{-1} for $[Eu(tta)_3(H_2O)_2]$.

3.3. Characterization of the films produced

FTIR data of the films are available in Figs. S2–S5. Comparing the doped films with the undoped polymer matrix, it is evident that the bands are primarily attributed to the matrix due to its major proportion in the film compositionx. TG/DTG/DTA data for the films are available in Fig. S12 in the supplementary material. All the samples used in the thermogravimetric studies are composed of films produced by casting with concentrations of 0.5 wt % and 5.0 wt %, the lower and higher limits of concentration on the production. The doped PMMA films have a similar thermal decomposition profile, with onset temperature of around 200 °C, different from isolated PMMA onset [36], which is

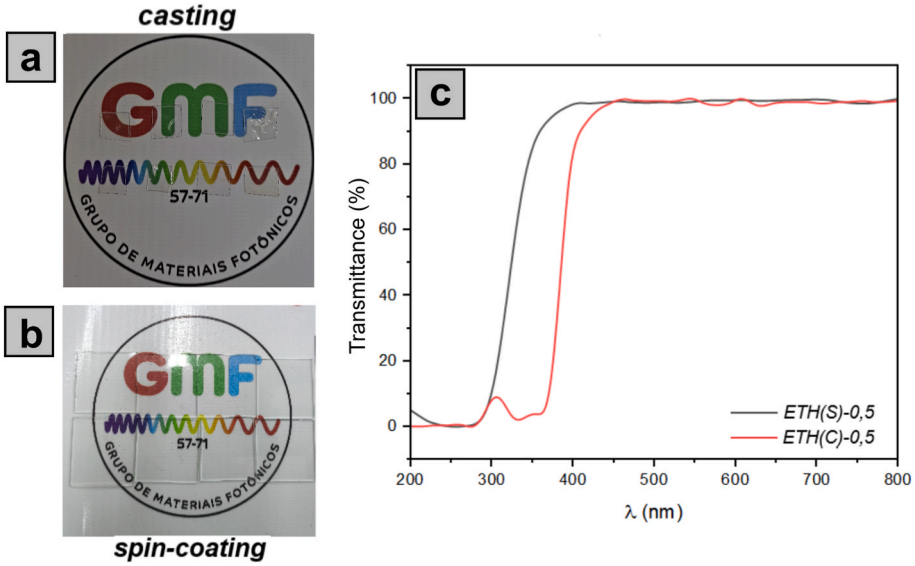

Fig. 6. Films produced via a) casting and b) spin coating, under ambient light and c) transmittance spectra of the ETH(C)-0.5 and ETH(S)-0.5 films.

around 240–250 °C, due to the decomposition of the organic ligands combined in the dopant complex. In this range, the $[Eu(tta)_3(amx)]$ doped films with 5.0 wt % concentration of complex shows less mass decomposition than the 0.5 wt % concentration films, which indicates the water absence in the dopant complex and the reduction of aggregate water on the produced films. A similar effect could be observed on the $[Eu(tta)_3(H_2O)_2]$, where, in the same range, shows a reduction of mass loss on the 5.0 wt % film compared with the 0.5 wt % film, but with one new thermal event in 250 °C, which could be associated with the coordinated water molecules on the europium complex. At 380 °C, PMMA self-ignites, with total degradation of the sample. In comparison with the films doped with $[Eu(tta)_3(H_2O)_2]$, films doped with $[Eu(tta)_3(amx)]$ presents a minor accentuated decomposition event at ~200 °C, associated with coordinated water molecules, which are absent in the ETA films. The data are conclusive that the $[Eu(tta)_3(amx)]$ films show higher thermal stability than $[Eu(tta)_3(H_2O)_2]$, due to the absence of coordination water mass decomposition, with best results in 5.0 wt % concentration.

The morphology of the films was evaluated via scanning electron microscopy (Fig. 4) and the roughness via atomic force microscopy, shown in Fig. 5 and Table 3. The SEM images of the ETH(C) and ETA(C) films show the surface of the films with protuberances and suspended particles, proportional to the increase in the dopant concentration, possibly generated in the solvent drying step of the polymer solution. Fig. 4 a), b), e), g) and h) films don't show major irregularities and are relatively homogeneous; the c) films show deformation waves, possibly due to the unmold process or during the acquisition of SEM data; and d) and f) films show greater irregularities due to different phases on the formation of the material. This effect can be associated with decrease solubility of the complex on the polymeric solution over the solvent evaporation step, and also affects the topology of the materials, which exhibit an increase in roughness proportional to the dopant concentration.

The quadratic roughness (R_q) data are found in Table 3. Despite having holes on the surface, the undoped PMMA film has a roughness (R_q) of 0.0025 μm, greater than some of the doped films. The R_q values of the doped films range from 0.0015 to 0.0253 μm, with the lowest R_q values attributed to the ETA films doped via spin coating. Furthermore, except for the ETH(C) films, all films showed an increase in R_q with increasing dopant concentration, due to the effect of particle concentration, as mentioned above. This trend are shown in Fig. 5, in which lower concentration films have less and smaller aggregates than films with higher concentration, which have more and greater aggregates.

3.4. Characterization and photophysical properties of films

From the transmittance spectrum of the films produced via casting and spin coating, Fig. 6c), it is notable that they have transparency above 95 % in the entire visible and NIR region, while in the UV region (<400 nm), the transmittance drops significantly. This characteristic can be observed in Fig. 6. It is also possible to observe differences between the curves of films produced by different methods, due to the difference in thickness [14], which varies from 40 to 130 μm on casting and from 0.8 to 5 μm on spin coating films. Film thickness data are presented in Table 3, and more detailed in Table S7. The transmittance pattern presented by the films is important, as it balances transparency, a prerequisite to produce optical materials [14], and shielding that guarantees UV protection, also extremely relevant in optical applications such as smart windows.

The UV–Vis electronic absorption data of the films reveals be similar with the absorption spectra of the complexes (Fig. S11) a main band with a maximum absorption wavelength at ~340 nm, referring to the $S_0 \rightarrow S_n$ transition of the organic ligands coordinated to Eu^{3+}, and a secondary band with a peak at ~275 nm. The increase in dopant concentration did not shift the bands, which suggests that there were no structural changes promoted by the effect of concentration on absorption.

The excitation and emission spectra of the films, are shown in Fig. 7, and the decay curves of the excited state are shown in Fig. S13. Regarding the electronic excitation data in the UV–Vis region, present in Fig. 7, the broad and intense bands in the near-UV region (250–400 nm) that dominate the excitation spectra, with λ_{max} around 395 nm for $[Eu(tta)_3(H_2O)_2]$, 380 nm for $[Eu(tta)_3(amx)]$ and 300–360 nm for the films (Fig. 7), is due to the π→π * transitions of the ligands 2-thenoyltrifluoroacetone and amoxicillin [37]. This is an indicative of the efficient absorption of ultraviolet radiation and energy transfer to the metallic center. The hypsochromic shift observed in the excitation peaks of the films compared to the complexes reveals the influence of the PMMA matrix on the energy absorption processes. Furthermore, the complexes exhibit excitation records associated with Eu^{3+} f-f transitions, namely: $^7F_0 \rightarrow {}^5L_6$, $^7F_0 \rightarrow {}^5D_2$ and $^7F_1 \rightarrow {}^5D_0$, revealing direct excitation of the metal, which does not appear in the film spectra, as the dominant transitions are those that occur only between ligands and metal.

About the emission spectra of the materials, presented in Fig. 7, in

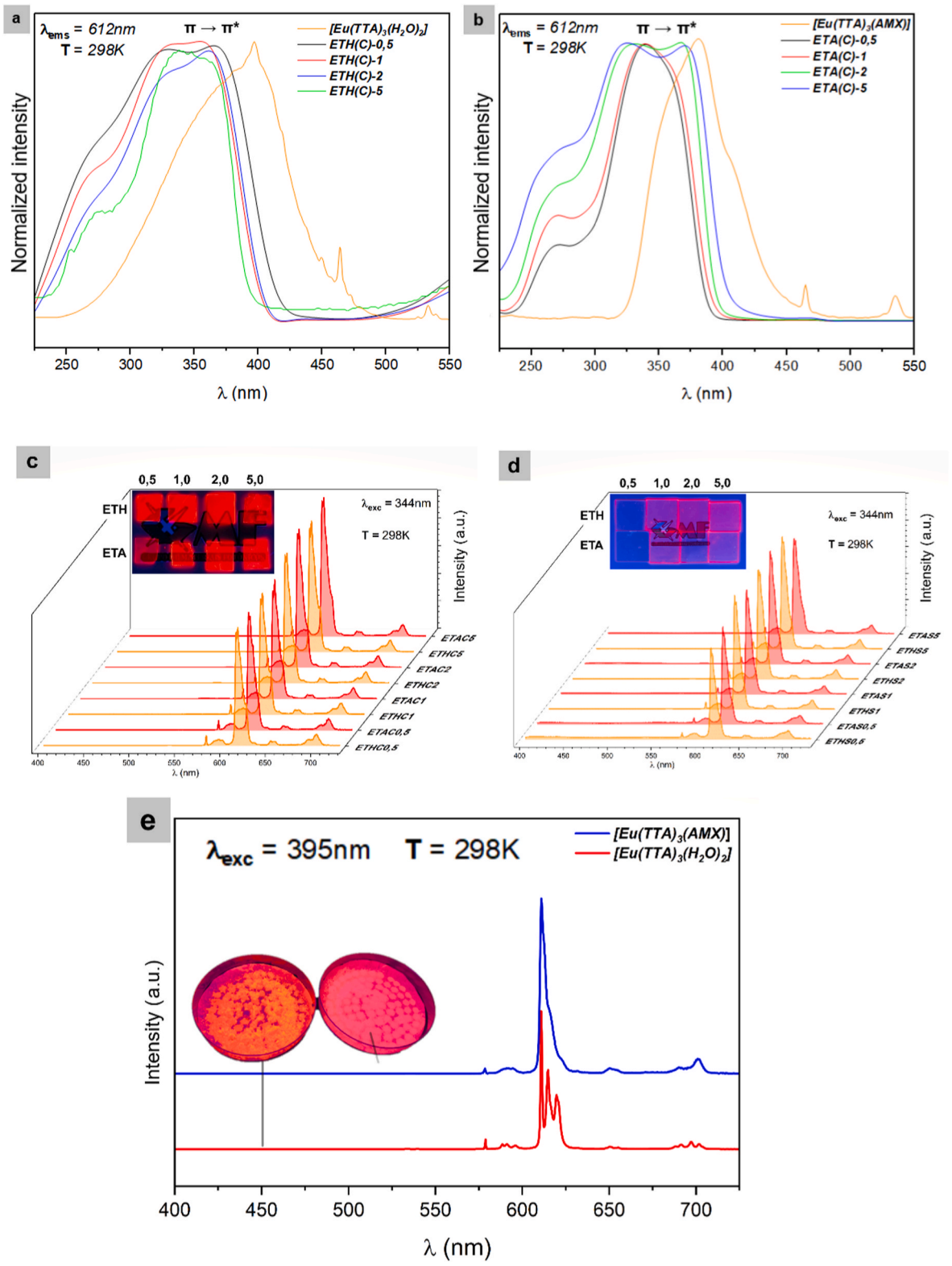

Fig. 7. Excitation spectra of the a) films doped with $[Eu(tta)_3(H_2O)_2]$, b) films doped with $[Eu(tta)_3(amx)]$ and emission spectra of the c) films produced by casting method, d) films produced by spin coating method.

every system show the main electronic transitions of Eu^{3+}, starting from the main emitter level $^5D_0$ non-degenerate to fundamental levels ^7F_J, namely $^5D_0 \rightarrow {}^7F_J$, with J = 0–4 [37].

The Judd-Ofelt intensity parameters (Ω_λ), radiative (A_{rad}) and non-radiative (A_{nrad}) decay rates, excited state lifetimes (τ) and chromaticity coordinates are found in Table S8. The increase in the lifetime of the $[Eu(tta)_3(amx)]$ complex and doped films compared to $[Eu(tta)_3(H_2O)_2]$ is mainly due to the reduction of the deactivation concerning the O-H oscillators present in water molecules. Furthermore, films produced via spin coating had longer lifetime values than films produced via casting, and did not show any correlation with dopant concentration. This effect is caused by the particle concentration, as

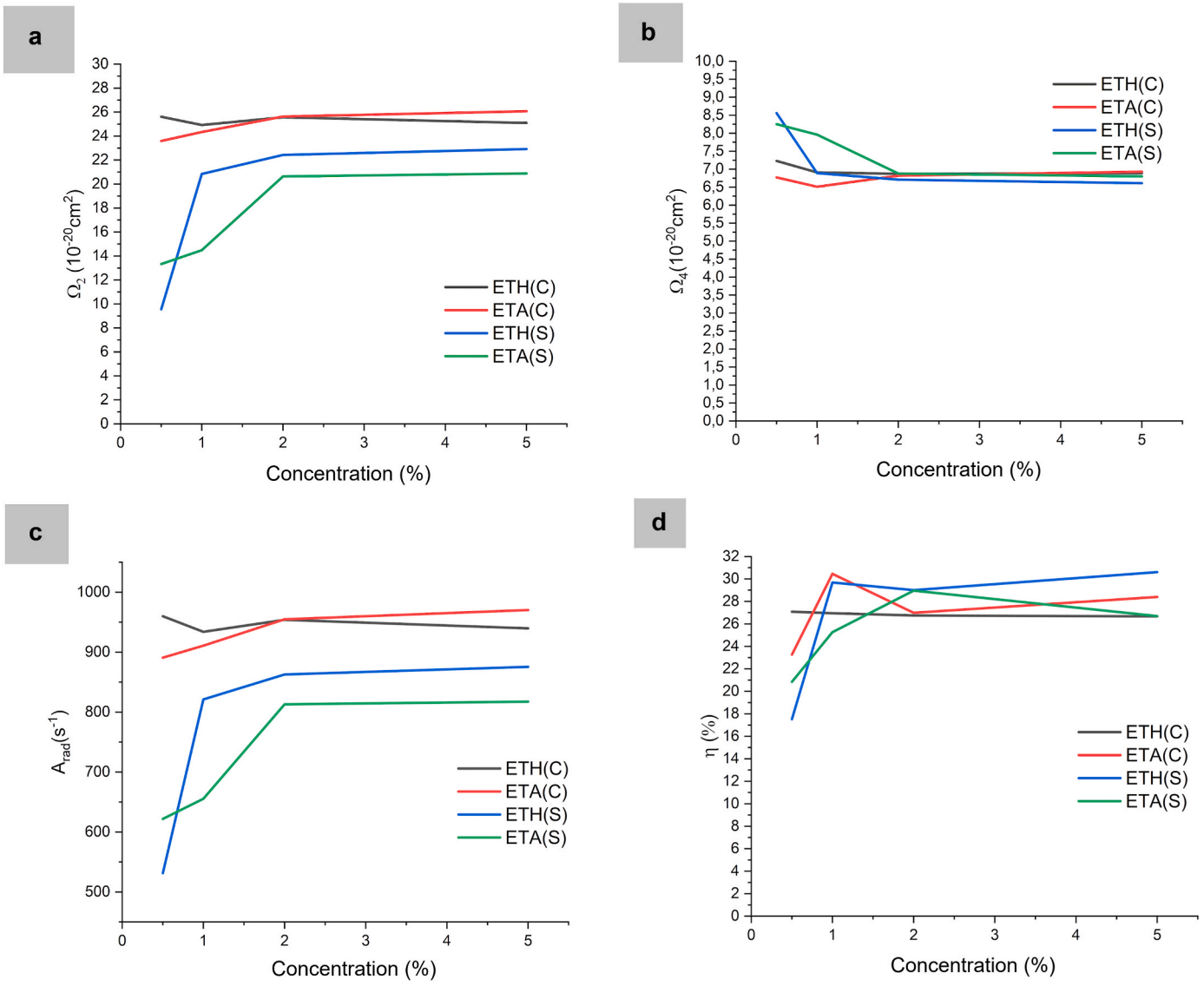

Fig. 8. Correlation curves of a) Intensity parameter Ω_2, b) Intensity parameter Ω_4, c) radiative decay rate and d) quantum efficiency as a function of concentration for the films.

shown in Figs. 4 and 5, where agglomerated particles of complex on the film keep each Eu^{3+} ion too close, resulting in a concentration suppression phenomenon, which slightly reduces the emission lifetime on films produced by drop casting method. This effect are not shown in films produced by spin coating method, what justify the difference in emission lifetime.

The intensity parameter Ω_2 is related to the transition $^5D_0 \rightarrow {}^7F_2$. Therefore, this parameter is associated with the polarizability of Eu^{3+}, being directly proportional to the covalence of the Eu^{3+}-ligand bond and asymmetry of the chemical environment. The parameters Ω_4 and Ω_6, on the other hand, related to the transitions $^5D_0 \rightarrow {}^7F_4$ and $^5D_0 \rightarrow {}^7F_6$, are associated with long-range interactions and rigidity of the structure, inversely proportional to the covalence of the bond metal-ligand, to the rigidity of the matrix to which the complex is anchored [38–42].

About the lifetime of the materials, the obtained curves indicate a monoexponential decay, according to the equation $I = I_0 e^{\left(-\frac{t}{\tau}\right)}$, reinforcing that each complex has only one symmetry site. The films produced via spin-coating exhibited longer lifetime values than those produced via casting. Both ETH and ETA films showed lifetimes that were only slightly dependent on the dopant concentration, with similar values for the same dopant and deposition method. This may be due to the nature of the interactions between Eu^{3+}/complex and the matrix.

The parameters Ω_2 of films produced by the casting method are, in general, higher than those of films produced via spin coating, nearing, but not reaching, the values of isolated complexes. Fig. 8 shows the variation profiles of the spectral parameters of the films.

In the ETH(C) films, as shown in Fig. 8a), the values of Ω_2, A_{rad} and η, the quantum eficiency, are very close, without showing significant variations in the concentration range studied. In ETA(C) films, a progressive increase in these values is observed, proportional to the concentration, which reveals that short-range disturbances can vary depending on the concentration. The parameter Ω_4, as seen in Fig. 8b), decreases in ETH(C) films, while in ETA(C) films they grow, proportionally to the concentration. In spin coating films, the parameter Ω_2 of the ETH(S) and ETA(S) systems, Fig. 8a), increases proportionally to the concentration. The parameter Ω_4 of both, Fig. 8b), however, varies, decreasing proportionally to the increase in concentration. The decrease in Ω_4 in the films with both dopants may indicate that when the concentration increases, the matrix influence under the metallic center become less pronounced, since a higher concentration corresponds to more volume around the complex, and there is no more involved only by

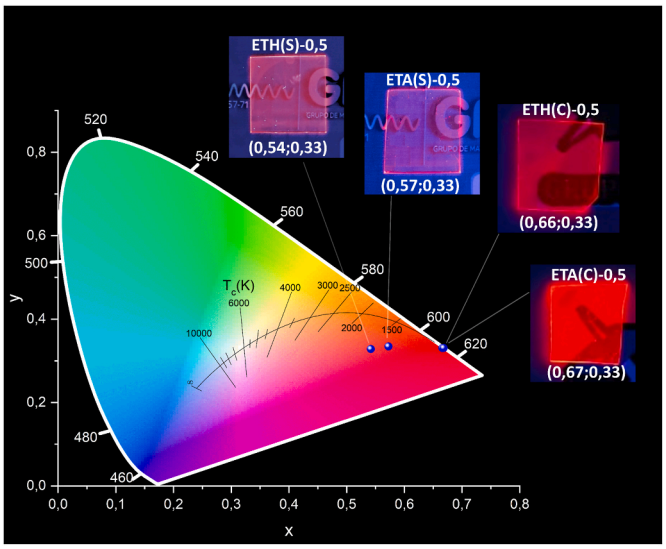

Fig. 9. CIE chromaticity diagram of the films ETH(S)-0.5, ETA(S)-0.5, ETH(C)-0.5 and ETA(S)-0.5.

the PMMA matrix, but by other units of the complex, generating a cross-interaction that reduces the influence on Eu^{3+} [21]. Finally, the data on A_{rad} and η, Fig. 8c) and d), grow proportionally to the concentration in systems with both dopants.

3.5. Colorimetry data

The photoluminescence data were used to determine the colorimetric properties (x, y) according to the parameters of the *Commission Internationale de l'Éclairage* (CIE) [43,44,45]. The colorimetric coordinates listed in the table are depicted in the chromaticity diagrams shown in Fig. 9.

The colorimetric data for the films produced via casting are very similar and increasing the dopant concentration does not significantly alter the color coordinates or affect the color purity. The films showed in Fig. 9 have the minimum concentration of dopant. Because of this, the intensity of the luminescence is visually lesser on the films produced by spin coating method, which results in color coordinates slightly tending to the PMMA isolated film color. But the films with higher concentration of dopant, as seen in Table S9, have more higher color purities, presenting visual color similarities, as predicted by the emission spectra. It's important to say that the emission of isolated PMMA is negligible, as seen on the emission spectra of all the systems.

CCT (Correlated Color Temperature) data was calculated for all the samples, but the data cannot be considered, because do not have their color coordinates within the Planckian locus, therefore, do not have representative CCT, based on the Δc data (<0.05) [43]. In contrast, for the films produced via spin coating, there is a noticeable trend where color purity increases proportionally with the dopant concentration, due to the higher luminescence intensity as the amount of complex present in the samples increases. However, no correlation is observed between dopant concentration and the dominant wavelength of radiation, suggesting that concentration only affects light intensity and color purity, rather than the wavelength of the radiation.

At a concentration of 0.5 wt %, the ETA(S) film exhibited better chromaticity data, namely: excitation purity, color purity, dominant wavelength, compared to the ETH(S) film, which was produced at the same concentration. This is significant as it indicates that a lower material concentration yields a more expressive color signature, as observed in Fig. 9.

The color purity and red purity of the ETH films are lower than those of the ETA films, as shown in Table S9. This suggests that in the case of ETA films, the dispersion of the new material within the matrix is more effective, resulting in a more expressive colorimetric response compared to the ETH films.

4. Conclusion

This work related the study of the new unprecedented material [Eu$(tta)_3(amx)$], in comparison with the hydrated complex [Eu$(tta)_3(H_2O)_2$], used as a precursor. As well, the ETH and ETA doped films, produced with a variation of the deposition method (casting and spin coating), complex and concentration (0.5 wt %, 1.0 wt %, 2.0 wt % and 5.0 wt %), was studied. The films revealed a series of important properties, including spectral, morphological and structural, for applications in luminescent devices and optical materials.

The emission spectra revealed an intense red luminescence of the complexes. The replacement of water molecules by the organic ligand amoxicillin in the new material [Eu$(tta)_3(amx)$] resulted in changes in spectral properties, such as changes in the local symmetry of Eu^{3+} and an increase in the rigidity of the structure, evidenced by the Judd-Ofelt intensity parameters. The new material is promising, as it improves the optical properties of the starting material by adding a low-cost binder, reducing production costs and increasing the added value of the final product.

The films produced have significant differences, highlighting the importance of the variables in the production procedure. Casting films present higher values of intensity parameters compared to spin coating films, which in turn presented uniform trends with increasing concentration, in addition to greater homogeneity and lower roughness. The dispersion capacity of the spin coating method is reflected in the film data, which follow better defined patterns than those produced via casting. Both films presented excellent transparency and characteristic Eu^{3+} emission data, which makes them excellent candidates for optoelectronic applications.

CRediT authorship contribution statement

Andrei Marcelino Sá Pires Silva: Writing – original draft, Visualization, Investigation, Formal analysis, Data curation, Conceptualization. **Airton Germano Bispo-Jr:** Writing – review & editing, Formal analysis, Data curation. **Fernando Aparecido Sigoli:** Writing – review & editing, Formal analysis, Data curation. **Carolina Ferreira de Matos Jauris:** Writing – review & editing, Formal analysis, Data curation. **Ernani Lacerda de Oliveira Neto:** Investigation, Formal analysis, Data curation. **Breno Pannia Espósito:** Formal analysis, Data curation. **Lilian Lefol Nani Guariero:** Formal analysis, Data curation. **Pollyana da Silva Melo:** Formal analysis, Data curation. **Ricardo Oliveira Freire:** Writing – review & editing, Methodology, Formal analysis, Data curation. **Jorge Fernando Silva de Menezes:** Writing – review & editing, Visualization, Supervision, Resources, Project administration, Funding acquisition, Formal analysis, Data curation.

Declaration of competing interest

The authors declare that they have no known competing financial interests or personal relationships that could have appeared to influence the work reported in this paper.

Acknowledgements

We acknowledge the Brazilian institutions CAPES (Fundação Coordenação de Aperfeiçoamento de Pessoal de Nível Superio), FAPESB (Fundação de Amparo à Pesquisa do Estado da Bahia), INCT-Energia & Ambiente and Institute of Science, Innovation, and Technology of the State of Bahia for Nanotechnology (FAPESB TO PIE0003/2022), INCT NanoVida, INCT- Nanocarbono for the financial support in carrying out this work. The author R.O.F. thanks CNPQ (grant n°. 306015/2022-6).

Appendix A. Supplementary data

Supplementary data to this article can be found online at https://doi.org/10.1016/j.jlumin.2025.121247.

Data availability

Data will be made available on request.

References

[1] Joseph A. Mattocks, A. Cotruvo Joseph, Biological, biomolecular, and bio-inspired strategies for detection, extraction, and separations of lanthanides and actinides, Chem. Soc. Rev. 49 (22) (2020) 8315–8334, https://doi.org/10.1039/D0CS00653J.

[2] Koen Binnemans, et al., Recycling of rare earths: a critical review, J. Clean. Prod. 51 (2013) 1–22, https://doi.org/10.1016/j.jclepro.2012.12.037.

[3] Tetsuro Jin, et al., Luminescence property of the terbium bipyridyl complex incorporated in silica matrix by a sol-Gel method, J. Electrochem. Soc. 142 (10) (1995) L195, https://doi.org/10.1149/1.2050043.

[4] F.A. Hart, F.P. Laming, Lanthanide complexes—III: complexes of 2, 2′-dipyridyl with lanthanide chlorides, thiocyanates, acetates and nitrates, J. Inorg. Nucl. Chem. 27 (8) (1965) 1825–1829, https://doi.org/10.1016/0022-1902(65)80326-8.

[5] Jing Feng, Hongjie Zhang, Hybrid materials based on lanthanide organic complexes: a review, Chem. Soc. Rev. 42 (1) (2013) 387–410, https://doi.org/10.1039/C2CS35069F.

[6] Andrey A. Knyazev, Aleksandr S. Krupin, Yuriy G. Galyametdinov, Luminescence behavior of PMMA films doped with Tb (III) and Eu (III) complexes, J. Lumin. 242 (2022) 118609, https://doi.org/10.1016/j.jlumin.2021.118609.

[7] Eny Kusrini, et al., Fluorescence properties of microcomposites europium triethylene glycol picrate complex doped in polymer, International Journal of Technology 5 (2014) 1, https://doi.org/10.14716/ijtech.v5i1.155.

[8] Kai, Jiang, et al., Intermolecular energy transfer and photostability of luminescence-tuneable multicolour PMMA films doped with lanthanide–β-diketonate complexes, J. Mater. Chem. 21 (11) (2011) 3796–3802, https://doi.org/10.1039/C0JM03474F.

[9] Jun Wang, et al., Self-assembled multilayer films of europium-substituted polyoxometalate and their luminescence properties, J. Alloys Compd. 376 (1–2) (2004) 68–72, https://doi.org/10.1016/j.jallcom.2004.01.004.

[10] Lin Zhang, et al., Preparation of polyacrylamide/nanosheets LYH: Eu nanocomposite film and enhanced photoluminescence, Opt. Mater. 108 (2020) 110437, https://doi.org/10.1016/j.optmat.2020.110437.

[11] Renata Reisfeld, et al., Intensification of luminescence of Europium-EDTA complex in polyvinyl pyrrolidone films by copper nanoparticles, Opt. Mater. 59 (2016) 3–7, https://doi.org/10.1016/j.optmat.2016.03.046.

[12] R.A.D.M. Ranashinghe, et al., Thin film formation of the polyvinylpyrrolidone-added europium tetrakis (Dibenzoylmethide)-Triethylammonium and its mechanoluminescent properties, in: Recent Global Research and Education: Technological Challenges: Proceedings of the 15th International Conference on Global Research and Education Inter-academia 2016, Springer International Publishing, 2017, https://doi.org/10.1007/978-3-319-46490-9_11.

[13] Thierry Pagnot, Pierre Audebert, Gilbert Tribillon, Photostability study of europium dibenzolymethide embedded in polystyrene thin films with high concentration, Chem. Phys. Lett. 322 (6) (2000) 572–578, https://doi.org/10.1016/S0009-2614(00)00478-4.

[14] Andrey A. Knyazev, Aleksandr S. Krupin, Yuriy G. Galyametdinov, Photostable temperature sensitive luminescent materials based on polystyrene doped by an anisometric Europium (III) complex, J. Lumin. 256 (2023) 119654, https://doi.org/10.1016/j.jlumin.2022.119654.

[15] R.G. Charles, R.C. Ohlmann, Europium thenoyltrifluoroacetonate, preparation and fluorescence properties, J. Inorg. Nucl. Chem. 27 (1) (1965) 255–259, https://doi.org/10.1016/0022-1902(65)80222-6.

[16] José Diogo L. Dutra, Thiago D. Bispo, Ricardo O. Freire, LUMPAC lanthanide luminescence software: efficient and user friendly, J. Comput. Chem. 35 (10) (2014) 772–775, https://doi.org/10.1002/jcc.23542.

[17] James JP. Stewart, MOPAC: a semiempirical molecular orbital program, J. Comput. Aided Mol. Des. 4 (1) (1990) 1–103, https://doi.org/10.1007/BF00128336.

[18] James J.P. Stewart. Stewart computational chemistry, 2007 net/, http://openmopac.

[19] Frank Neese, The ORCA program system, Wiley Interdiscip. Rev. Comput. Mol. Sci. 2 (1) (2012) 73–78, https://doi.org/10.1002/wcms.81.

[20] Gerd B. Rocha, et al., Rm1: a reparameterization of am1 for h, c, n, o, p, s, f, cl, br, and i, J. Comput. Chem. 27 (10) (2006) 1101–1111, https://doi.org/10.1002/jcc.20425.

[21] Manoel AM. Filho, et al., RM1 model for the prediction of geometries of complexes of the trications of Eu, Gd, and Tb, J. Chem. Theor. Comput. 10 (8) (2014) 3031–3037, https://doi.org/10.1021/ct400909w.

[22] Jr Holtzclaw, F. Henry, P. Collman James, Infrared absorption of metal chelate compounds of 1, 3-diketones1, J. Am. Chem. Soc. 79 (13) (1957) 3318–3322, https://doi.org/10.1021/ja01570a006.

[23] D. Purushotham, V. Ramachanda Rao, BHSV Raghava Rao, Studies on rare earth 1, 3-diketonates, Anal. Chim. Acta 33 (1965) 182–197, https://doi.org/10.1016/S0003-2670(01)84873-X.

[24] Robert West, Reed Riley, The infra-red spectra of metal acetylacetonates in the sodium chloride region, J. Inorg. Nucl. Chem. 5 (4) (1958) 295–303, https://doi.org/10.1016/0022-1902(58)80007-X.

[25] L.J. Bellamy, R.F. Branch, The infra-red spectra of chelate compounds. Part II. Metal chelate compounds of β-diketones and of salicylaldehyde, J. Chem. Soc. (1954) 4491–4494, https://doi.org/10.1039/JR9540004491.

[26] Ralph G. Pearson, Hard and soft acids and bases, J. Am. Chem. Soc. 85 (22) (1963) 3533–3539, https://doi.org/10.1021/ja00905a001.

[27] Albert E. Bird, Amoxicillin, Anal. Profiles Drug Subst. Excipients 23 (1994) 1–52, https://doi.org/10.1016/S0099-5428(08)60599-7. Academic Press.

[28] Andreea Bebu, et al., IR, Raman, SERS and DFT study of amoxicillin, J. Mol. Struct. 993 (1–3) (2011) 52–56, https://doi.org/10.1016/j.molstruc.2010.11.067.

[29] Catherine Bisson-Boutelliez, et al., Preparation and physicochemical characterization of amoxicillin β-cyclodextrin complexes, AAPS PharmSciTech 11 (2010) 574–581, https://doi.org/10.1208/s12249-010-9412-1.

[30] M.A. Zayed, S.M. Abdallah, Synthesis and structure investigation of the antibiotic amoxicillin complexes of d-block elements, Spectrochim. Acta Mol. Biomol. Spectrosc. 61 (9) (2005) 2231–2238, https://doi.org/10.1016/j.saa.2004.08.022.

[31] J.F.S. de. Menezes. Estudo fotoluminescente de tristenoiltrifluoroacetanatos de lantanídeos com sulfóxidos (Tese (Doutorado), Universidade de São Paulo, São Paulo, 1999.

[32] Diogo Alves Gálico, et al., Solid state thermal and spectroscopic studies on the antibiotic amoxicillin trihydrate, Brazilian Journal of Thermal Analysis 2 (1) (2013) 45–49, https://doi.org/10.18362/bjta.v2i1.10.

[33] M.A. Hussien, Samy M. El-Megharbel, Moamen S. Refat, Spectroscopic and molecular structure characterization of Cu (II), Co (II), Ni (II) and Fe (III) amoxicillin antibiotic drug complexes in alcoholic media, J. Mol. Liq. 221 (2016) 61–71, https://doi.org/10.1016/j.molliq.2016.05.050.

[34] Moamen S. Refat, et al., Synthesis, thermal and spectroscopic behaviors of metal–drug complexes: La (III), Ce (III), Sm (III) and Y (III) amoxicillin trihydrate antibiotic drug complexes, Spectrochim. Acta Mol. Biomol. Spectrosc. 128 (2014) 427–446, https://doi.org/10.1016/j.saa.2014.02.160.

[35] Rida Masmoudi, et al., Theoretical study of the degradation of Amoxicillin by interaction with the hydroxyl radical (. OH), J. New Technol. Mater. 11 (01) (2021) 63–80.

[36] Alain Alonso, et al., Self-heating evaluation on thermal analysis of polymethyl methacrylate (PMMA) and linear low-density polyethylene (LLDPE), J. Therm. Anal. Calorim. 147 (18) (2022) 10067–10081, https://doi.org/10.1007/s10973-022-11364-x.

[37] Koen Binnemans, Interpretation of europium (III) spectra, Coord. Chem. Rev. 295 (2015) 1–45, https://doi.org/10.1016/j.ccr.2015.02.015.

[38] Wenqin Luo, et al., Determination of Judd–Ofelt intensity parameters from the excitation spectra for rare-earth doped luminescent materials, Phys. Chem. Chem. Phys. 12 (13) (2010) 3276–3282, https://doi.org/10.1039/B921581F.

[39] Christian K. Jørgensen, Renata Reisfeld, Judd-Ofelt parameters and chemical bonding, Journal of the Less Common Metals 93 (1) (1983) 107–112, https://doi.org/10.1016/0022-5088(83)90454-X.

[40] W.T. Carnall, P.R. Fields, K. Rajnak, Spectral intensities of the trivalent lanthanides and actinides in solution. II. Pm3+, Sm3+, Eu3+, Gd3+, Tb3+, Dy3+, and Ho3+, J. Chem. Phys. 49 (10) (1968) 4412–4423, https://doi.org/10.1063/1.1669892.

[41] SG Prasanna Kumar, et al., Understanding the photoluminescence behaviour in nano CaZrO3: Eu3+ pigments by Judd-Ofelt intensity parameters, Dyes Pigments 150 (2018) 306–314, https://doi.org/10.1016/j.dyepig.2017.12.022.

[42] L.G. Van Uitert, Characterization of energy transfer interactions between rare earth ions, J. Electrochem. Soc. 114 (10) (1967) 1048, https://doi.org/10.1149/1.2424184.

[43] Janos Schanda, Colorimetry: Understanding the CIE System, John Wiley & Sons Press, 2007, https://doi.org/10.1002/9780470175637.

[44] Daniel Malacara, Color Vision and Colorimetry: Theory and Applications, Spie, Bellingham, WA, USA, 2011, https://doi.org/10.1117/3.881172.

[45] Noboru Ohta, Alan Robertson, Colorimetry: Fundamentals and Applications, John Wiley & Sons, 2006, https://doi.org/10.1002/0470094745.